Gyrokinetic simulation of low-n Alfvénic modes in tokamak HL-2A plasmas

Wen-Hao Lin(林文浩)[1], Ji-Quan Li(李继全)[1,†], J Garcia[2], and S Mazzi[3]

[1] *Southwestern Institute of Physics, Chengdu* 610041, *China*
[2] *CEA, IRFM,* 13108, *Saint-Paul-lez-Durance, France*
[3] *EPFL, Swiss Plasma Center, Lausanne, Switzerland*

(Received 15 February 2022; revised manuscript received 23 April 2022; accepted manuscript online 28 April 2022)

The turbulence characteristics of plasmas with internal transport barriers in the HL-2A tokamak are analyzed by means of linear gyrokinetic simulations. It is found that turbulence is dominated by the ion temperature gradient (ITG) mode together with large-scale modes characterized by high-frequency electromagnetic fluctuation, which are destabilized by the steep ion temperature gradient in the weak magnetic shear regime. Comparison with solutions of analytical dispersion relations shows that their linear features match well with the beta-induced Alfvén eigenmode branch of the shear Alfvénic spectrum. It is further clarified that the large population of fast ions in these plasmas plays a stabilization role through the dilution mechanism in high-n ITG mode regimes.

Keywords: low-n Alfvénic modes, fast ions, gyrokinetic simulation, tokamak

PACS: 52.35.–g, 52.35.Bj, 52.55.Pi, 52.65.Tt **DOI:** 10.1088/1674-1056/ac6b23

1. Introduction

Recently, various fast-ion-related experimental observations[1,2] in the Joint European Torus (JET) and related numerical studies[3–7] have highlighted the beneficial role of fast ions in reducing turbulent transport and improving confinement. There are many promising linear explanations for the beneficial impact of fast ions on overall plasma confinement, such as resonance interaction between fast ions and bulk plasma turbulence,[7] but these mechanisms are still incapable of explaining the substantial reduction in the ion profile 'stiffness' parameter,[3] a quantity defined as the ratio of ion heat flux to the logarithmic ion temperature gradient and indicating the level of transport driven by plasma turbulence. Another competitive mechanism proposed for such transport reduction has been studied numerically with the GENE code,[8] highlighting the nonlinear interplay between marginally stable fast-ion-induced Alfvénic activities and bulk plasma microturbulence, for example the ion temperature gradient (ITG) mode. The role of linearly marginally unstable low-n modes, identified as the toroidicity-induced Alfvén eigenmode (TAE) in JET plasmas, was emphasized.

Further experiments have shown that strong reduction of turbulent ion heat transport, reaching conditions for transport suppression, occurs with a TAE that is fully destabilized by MeV ions, as expected in ITER with alpha particles but generated by ion cyclotron resonant heating (ICRH) in the case of JET.[9–11] A strong interplay between TAE modes and zonal flows, highly dependent on electromagnetic effects, is found in non-linear gyrokinetic simulations in these conditions.[11] In turn, zonal flows reduce turbulent transport driven by the ITG, leading to improved thermal confinement.

The fact that ion heat transport may be suppressed by the interplay between high-frequency low-n modes destabilized by fast ions and ITG turbulence, opens up the possibility that such a mechanism has played a role in experiments in which internal transport barriers (ITBs) are formed in the presence of a strong fast-ion-generated population. This could be the case for recent discharges of the HL-2A tokamak with high-power neutral beam injection (NBI),[12] in which the plasmas are characterized by a low electron density and a significantly larger portion of fast ions compared with JET plasma. In particular, ITB in the ion temperature profile is formed with weakly reversed magnetic shear in the core plasma. However, the possibility that fast ion effects play a role as an underlying physical mechanism for ITB triggering has never been clarified. To gain a better understanding of the impact of fast ions on HL-2A plasmas with ITB, linear gyrokinetic simulations based on a local version of the GENE code[8] are carried out in this work. Emphasis is given to mode characterization and GENE validation in such plasmas when fast ions are included in/excluded from the simulations. This is an important step, as plasmas analyzed in JET are not of the same nature as in HL-2A. Notably, the magnetic shear is higher and the ion temperature gradient lower for JET than for HL-2A, which might lead to significant differences in terms of turbulence characteristics.

The remainder of this paper is organized as follows. In

†Corresponding author. E-mail: lijq@swip.ac.cn

© 2023 Chinese Physical Society and IOP Publishing Ltd

Section 2, the physical model used in the GENE code is briefly described and the simulation setup and input parameters from HL-2A discharge #22453 are arranged. Section 3 is devoted to the linear GENE simulation and stability analysis in HL-2A plasmas with or without fast ions. Simulation results are comprehensively compared with the numerical solutions of the general fish-bone-like dispersion relation (GFLDR) derived by Zonca *et al.*[13] Finally, the main results in this work are summarized in Section 4.

2. Physical model in the GENE code and numerical setup

Numerical simulations in this work are performed using a local version of the GENE code, which works in field-aligned coordinates with (x, y, z) corresponding to the radial, binormal and parallel directions, respectively. In GENE's linear local version, the normalized gyrokinetic Vlasov equation for the perturbed distribution function f_{1j} of species j reads[22,23]

$$\begin{aligned}\frac{\partial g_j}{\partial t} &= \mathrm{i}k_y\left[\omega_{nj}+\omega_{Tj}(v_\parallel^2+\mu B_0-3/2)\right]\bar{\chi}_{1j}f_{0j}\\ &-\mathrm{i}\frac{T_{0j}}{Z_j}\left[(2v_\parallel^2+\mu B_0)\frac{(\boldsymbol{k}_\perp\times\boldsymbol{B}_0)\cdot\nabla B_0}{B_0^3}-v_\parallel^2\beta_\mathrm{e}\frac{p_0}{B_0^2}\omega_\mathrm{p}k_y\right]\Gamma_j\\ &-\frac{v_{Tj}v_\parallel}{JB_0}\frac{\partial}{\partial z}\Gamma_j+\frac{v_{Tj}}{2}\frac{\mu\partial_z B_0}{JB_0}\frac{\partial}{\partial v_\parallel}f_{1j}+\langle C_j(f)\rangle,\end{aligned}\tag{1}$$

while the Poisson (quasi-neutrality) equation and the parallel Ampère law respectively are

$$\begin{aligned}&\sum_j \pi n_j Z_j\int B_0\bar{f}_{1j}\,\mathrm{d}v_\parallel\,\mathrm{d}\mu\\ &=\sum_j\frac{Z_j^2 n_j}{T_j}\left(\phi_1-\int B_0\overline{\overline{\phi}}_1\,\mathrm{e}^{-\mu B_0}\,\mathrm{d}\mu\right),\end{aligned}\tag{2}$$

$$\sum_j\frac{\beta_\mathrm{e}}{2}v_{Tj}\pi n_j Z_j\int B_0\bar{f}_{1j}v_\parallel\,\mathrm{d}v_\parallel\,\mathrm{d}\mu=k_\perp^2 A_{1\parallel}.\tag{3}$$

Here equilibrium quantities and perturbed quantities are denoted with the subscripts '0' and '1', respectively. A bar above quantities represents gyro-average operation. The modified distribution function

$$g_j=f_{1j}+v_{Tj}v_\parallel\bar{A}_{1\parallel}\frac{Z_j}{T_{0j}}f_{0j}\tag{4}$$

is defined to unite the time derivatives of f_{1j} and $A_{1\parallel}$ in one quantity (which facilitates time discretization), while the modified potential

$$\bar{\chi}_{1j}=\bar{\phi}_1+\frac{T_{0j}}{Z_j}\mu\bar{B}_{1\parallel}-v_{Tj}v_\parallel\bar{A}_{1\parallel}\tag{5}$$

contains the gyro-averaged potential ϕ_1, parallel vector potential $A_{1\parallel}$ and parallel magnetic fluctuation $B_{1\parallel}$. The non-adiabatic part of f_{1j} is defined as

$$\Gamma_j=f_{1j}+\frac{Z_j}{T_{0j}}f_{0j}\bar{\phi}_1.\tag{6}$$

The normalized logarithmic gradient of a quantity (e.g., T_e the electron temperature) is defined as

$$\omega_{T_\mathrm{e}}=\frac{L_\mathrm{ref}}{L_{T_\mathrm{e}}}=-\frac{L_\mathrm{ref}}{T_\mathrm{e}}\frac{\mathrm{d}T_\mathrm{e}}{\mathrm{d}x}\tag{7}$$

with the reference length L_ref being the minor radius a in this work. For the sake of completeness, the parallel magnetic fluctuation $B_{1\parallel}$ is preserved and the linearized Landau–Boltzmann collision model[14] is employed for the collisional term $\langle C_j(f)\rangle$ in Eq. (1), but their effects are actually negligible for the presentation of the simulation results, as will be justified in Subsection 3.2 where we reproduce simulation results with acceptable error neglecting the effects of $B_{1\parallel}$ and collision. The definitions of other quantities and the rules for normalization can be found in Refs. [22,23]. Unless otherwise specified, EFIT equilibrium is employed and all the species are treated as fully kinetic. For simplicity, the equilibrium velocity distribution f_0 of all species (including fast ions) is chosen to be Maxwellian.

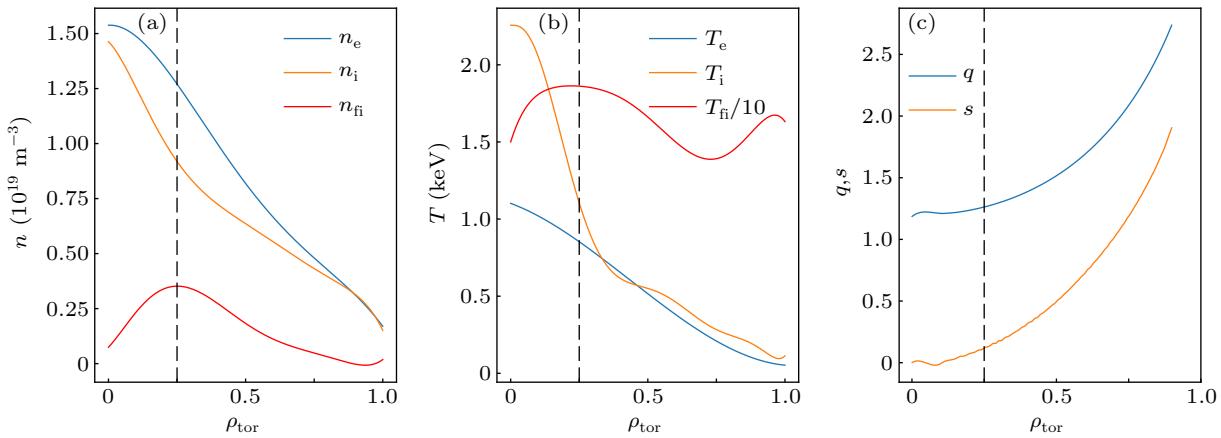


Fig. 1. Profiles of plasma density (a), temperature (b) and safety factor and magnetic shear (c) in HL-2A discharge #22453.

The profiles shown in Fig. 1 roughly describe the plasma state at time slice 650 ms in ITB discharge shot #22453. The black dashed lines indicate where the flux-tube simulation domain locates radially. These profiles were reconstructed using the kinetic-EFIT equilibrium code. The thermal and fast ions are both chosen to be hydrogen and are denoted with subscripts 'i' and 'fi', respectively. Note that the fast ion profiles have been multiplied by some number for readability. The shape of the electron density profile is assumed to be the same as that of the similar discharge #25733.[12] The electron and thermal ion temperature profiles are measured through electron cyclotron emission[15] and charge exchange recombination[16] diagnosis systems, respectively. Fast ion profiles are output from NUBEAM[17] calculation. The simulation box is chosen to be located at the ITB region $x_0 = 0.25a$. Corrugation of the profiles can be found near $\rho_{\rm tor} = 0$ and 1.0, which is caused by both the uncertainty of measurement and the error of interpolation. However, this problem is not severe at the simulation flux-tube domain $\rho_{\rm tor} = 0.25$. The grid resolutions in the radial, parallel, parallel velocity and magnetic moment dimension are $(n_x, n_z, n_{v_\parallel}, n_w) = (48, 32, 32, 16)$. Thirty-two binormal wave numbers k_ys are used, with each of them corresponding to toroidal number n from 1 to 32 under the relation $k_y = nq_0/x_0$. The safety factor $q_0 = 1.26$ and magnetic shear $\hat{s} = 0.12$ are calculated from the kinetic EFIT equilibrium reconstruction at $\rho_{\rm tor} = 0.25$. Note that the q profile is set as a proportional function of the magnetic shear in the local version of GENE, so the q profile used in local simulations is expressed as $q = q_0[1 + \hat{s}(x - x_0)/x_0]$, where $x = a\rho_{\rm tor}$ is the radial coordinate and x_0 is the radial location of the flux-tube. $\hat{s}$–α geometry[18] is also employed in this work to facilitate comparisons with the analytical formula introduced below. The radial extension of the simulation box for each toroidal number n is $l_x = 1/(k_y\hat{s}) \approx 260\rho_{\rm i}/n$. Other dimensionless parameters used in the simulations with and without fast ions can be found in Table 1. In the following, linear local GENE simulations will be performed for the case with and without fast ions, denoted by 'WFI' and 'NFI', respectively. Also, the GFLDR will be solved for the NFI case in Table 1.

Table 1. Input local parameters for GENE simulations. The nomenclature is conventional. The electron density $n_{\rm e}$, temperature $T_{\rm e}$ and minor radius a are used as reference quantities ($n_{\rm e} = 1.271 \times 10^{19}$ m^{-3}, $T_{\rm e} = 0.853$ keV and $a = 0.358$ m). The cases with fast ions and no fast ions are denoted by WFI and NFI, respectively.

HL-2A discharge #22453					
$n_{\rm i}/n_{\rm e}$ (NFI)	$n_{\rm i}/n_{\rm e}$ (WFI)	$n_{\rm fi}/n_{\rm e}$	$T_{\rm i}/T_{\rm e}$	$T_{\rm fi}/T_{\rm e}$	$a/L_{n_{\rm e}}$
1.0	0.72	0.28	1.29	22.22	1.39
$a/L_{n_{\rm i}}$ (NFI)	$a/L_{n_{\rm i}}$ (WFI)	$a/L_{n_{\rm fi}}$	$a/L_{T_{\rm e}}$	$a/L_{T_{\rm i}}$	$a/L_{T_{\rm fi}}$
1.39	1.85	0.16	1.48	5.20	0.34
a/R_0	B_0 (T)	q_0	$\hat{s}$	$\beta_{\rm e}$	α
0.21	1.34	1.26	0.12	0.242%	0.207

3. Stability analysis in HL-2A plasma

GENE simulations of linear instability were carried for a NBI-heated HL-2A plasma with an ion ITB. The normalization rules follow the GENE convention with sound frequency $\omega_{\rm ref} \approx 2\pi \cdot 127$ kHz and gyro-radius $\rho_{\rm ref} \approx a/160$, calculated from the sound velocity. Note that each k_y point in this case corresponds to the toroidal number n from 1 to 32. Results of linear simulations with fast ions excluded and included are shown in Fig. 2. For convenience of illustration, the diamagnetic frequency $\omega_{*\rm pi} = \omega_{*\rm ni} + \omega_{*\rm Ti} = k_y T_{\rm i}(a/L_{n_{\rm i}} + a/L_{T_{\rm i}})/(eB_0 a)$ and the kinetic thermal ion (KTI) gap frequency[19] $\omega_{\rm KTI} = \omega_{\rm ti} q_0 (7/4 + T_{\rm e}/T_{\rm i})^{1/2}$ (where $\omega_{\rm ti} = (2T_{\rm i}/m_{\rm i})^{1/2}/(q_0 R_0)$ is the ion transit frequency) are also plotted in Fig. 2(b).

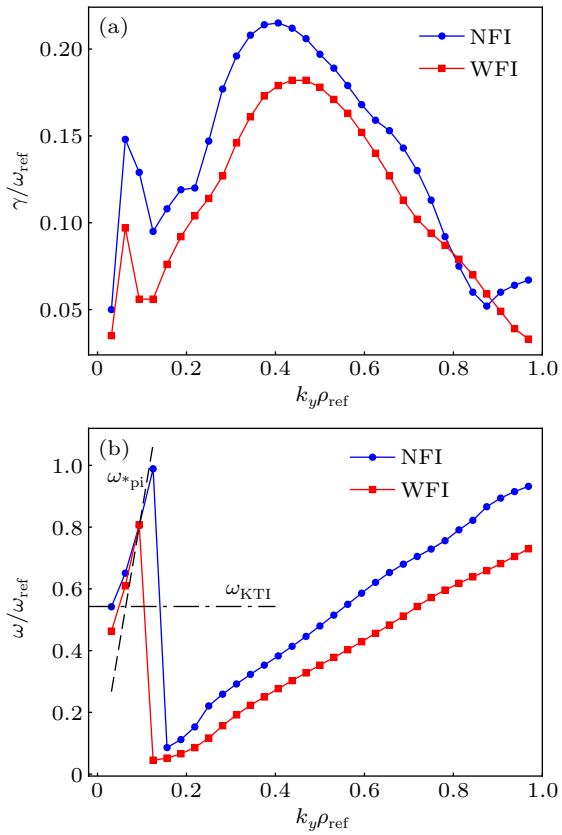


Fig. 2. The growth rate (a) and frequency (b) for HL-2A cases with fast ions (WFI) and no fast ions (NFI).

3.1. The case without fast ions

It can be seen that for the range $0.2 < k_y < 1$, the spectrum is dominated by modes with frequencies in the ion diamagnetic drift direction. We claim that these modes are ITG modes since their frequencies and growth rates can be reproduced by the ITG dispersion relation shown in next subsection. The most noteworthy point here is that a high-frequency mode appears in the low-n range, which also propagates along the direction of ion diamagnetic drift. Since these low-n high-frequency modes are fully excited without fast ions (shown by the blue curve in Fig. 2), these low-n modes may also exist

in the absence of NBI heating. As seen in Fig. 2(b), frequencies of these modes are far below the TAE frequency (according to Eq. (30) in Ref. [19], $\omega_{\rm TAE} = 2.42\omega_{\rm ref}$ for our case) and comparable to both the diamagnetic frequency $\omega_{*\rm pi}$ and the transit frequency $\omega_{\rm ti}$, which may imply a strong coupling of the kinetic ballooning mode (KBM) and the beta-induced Alfvén eigenmode (BAE).[13] Their mode structures of potential ϕ in ballooning coordinate χ, as shown in Fig. 3(a) (taking the $n = 4$ mode as an example), display a two-scale dependence. One small-scale fluctuation varies on $\chi \sim O(1)$ while the whole potential varies on a large scale. Meanwhile, these low-n modes are uniformly located in the poloidal direction without visible ballooning structure, as displayed in Fig. 3(b). Besides, the effective magnetic potential ψ is also shown in Fig. 3(a), which is calculated from GENE's direct output of the parallel vector potential $A_\parallel$ and the Jacobian J of the field-aligned coordinate using the relation

$$\psi(\chi) = \mathrm{i}\omega \int_{-\infty}^{\chi} JB_0 A_\parallel \,\mathrm{d}\chi' + \text{const.} \tag{8}$$

It can be seen that this effective potential ψ matches well with the potential ϕ, which indicates that the parallel electric field fluctuation

$$E_\parallel = -\frac{1}{JB_0}\frac{\mathrm{d}}{\mathrm{d}\chi}(\phi - \psi) \tag{9}$$

is nearly zero, characterizing the ideal magnetohydrodynamic (MHD) limit and a fully electromagnetic mode.

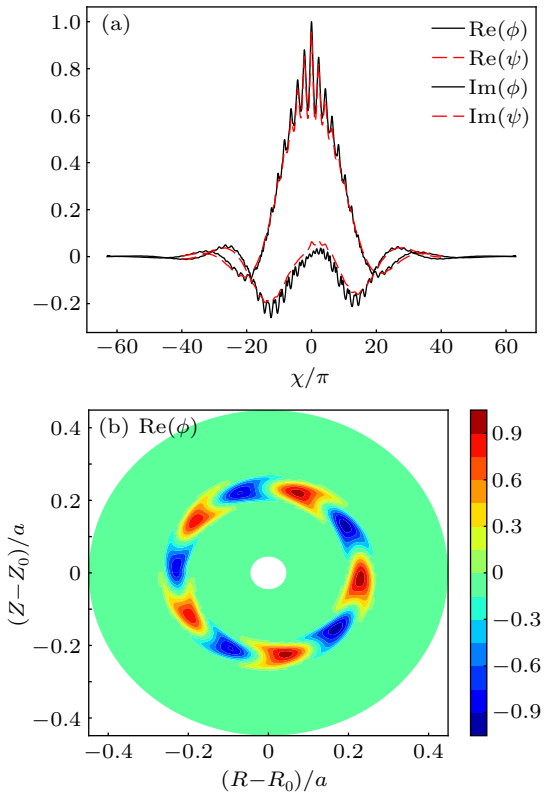


Fig. 3. (a) Electrostatic potential ϕ and effective magnetic potential ψ in ballooning representation and (b) the real part of potential ϕ in poloidal cross section.

To further elaborate the linear stability features of the low-n modes above and investigate their parametric dependence, the ratio of plasma pressure and magnetic pressure β, the magnetic shear $\hat{s}$ and logarithmic ion temperature gradient $a/L_{T_{\rm i}}$ are scanned. As shown in Figs. 4(a1) and 4(a2), these low-n modes are destabilized at low β combined with low $\hat{s}$. This may characterize the condition under which the low-n 'infernal modes' emerge, as pointed out in Ref. [20]. However, the phenomenon of frequency oscillations with increasing n is not observed here, implying that these low-n modes should not share the same properties of the infernal modes described in Ref. [20]. Besides, as seen in Fig. 4(c), finite ion temperature gradient $a/L_{T_{\rm i}}$ is required to destabilize these low-n modes. The critical stability thresholds $a/L_{T_{\rm i}}$ of these modes are roughly proportional to $1/n$. Note that the actual critical $a/L_{T_{\rm i}}$ of the $n = 4$ mode is obscure here because the $n = 4$ mode should disappear near the threshold. However, the $n = 4$ mode is unstable with a finite growth rate, indicating that this component is also characterized by the ITG mode.

Inspired by the linear properties of these low-n modes and considering that their frequencies are located in the range of $\omega \sim \omega_{*\rm pi} \sim \omega_{\rm KTI}$, the GENE simulations are compared with the solutions of the GFLDR from Ref. [19]. Including both ion compressibility and the ion diamagnetic drift effect on the left-hand side of the GFLDR while neglecting the kinetic contribution of fast ions on the right-hand side, the GFLDR is written as follows:[13]

$$\mathrm{i}\Lambda = \delta W_{\rm f}, \tag{10}$$

where

$$\Lambda = \left\{ \frac{\omega^2}{\omega_{\rm A}^2}\left(1 - \frac{\omega_{*\rm pi}}{\omega}\right) + q^2 \frac{\omega\omega_{\rm ti}}{\omega_{\rm A}^2}\left[1 - \frac{\omega_{*\rm ni}}{\omega}F\left(\frac{\omega}{\omega_{\rm ti}}\right) - \frac{\omega_{*\rm Ti}}{\omega}G\left(\frac{\omega}{\omega_{\rm ti}}\right) - \frac{N^2(\omega/\omega_{\rm ti})}{D(\omega/\omega_{\rm ti})}\right]\right\}^{1/2}. \tag{11}$$

In Eq. (11), all the frequencies are the same as defined above and F, G, N, D are transcendental functions whose definition can be found in Ref. [13]. Equation (10) is a unified dispersion relation describing two separate branches of the low-frequency surface acoustic wave (SAW) spectrum, i.e., the KBM and BAE branches, coupled with each other when $a/L_{T_{\rm i}} \neq 0$. After a straightforward input of the frequency in the left-hand side, Eq. (10) is solved near the accumulation point so that $\delta W_{\rm f} \to 0$, since the low-n modes have ideal MHD properties, as mentioned above. Meanwhile, since $q_0 = 1.26$ here the parallel wave number $k_\parallel qR = nq - m$ is typically finite. This means that there is no unstable continuous spectrum near the accumulation point in HL-2A plasma and therefore that $\delta W_{\rm f}$ could be arbitrarily assumed to be a small and negative

value. This assumption is valid since near $\delta W_{\rm f} \to 0$ the solutions of the GFLDR are unsusceptible to the change of $\delta W_{\rm f}$, as is explained in Ref. [13] and shown in Fig. 4. The solutions of the GFLDR assuming $\delta W_{\rm f} = -0.01$ and the results of GENE simulations using EFIT equilibrium and $\hat{s}$–α geometry are plotted in Fig. 5. Note that there are multiple solutions for the transcendental equation (10), so the solutions near $(\omega_{\rm ref}/2, \omega_{\rm ref}/2)$ in the complex plane with a maximal growth rate are chosen to obtain the GFLDR spectrum. Comparison indicates that the GFLDR formula can qualitatively capture the spectral features of the low-n modes. Furthermore, the GFLDR result is much better in agreement with the GENE simulation based on the $\hat{s}$–α geometric model. This observation is reasonable since the GFLDR is also derived using the $\hat{s}$–α geometry.

To further confirm the affinity between GFLDR solutions and the GENE simulation results, the simulations in Fig. 4(c) were performed again using $\hat{s}$–α geometry; the results are shown in Fig. 6. The critical $a/L_{T_{\rm i}}$ in GENE simulations is compared with the analytical prediction of the stability threshold of the BAE branch (i.e., Eq. (32) in Ref. [13]),

$$a/L_{T_{\rm i}}|_{\rm critical} = \frac{1}{q_0\sqrt{7/4+T_{\rm e}/T_{\rm i}}}\frac{\omega_{\rm ti}}{\omega_{*{\rm ni}}}\frac{a}{L_{n_{\rm i}}}. \tag{12}$$

This critical value is shown in Fig. 6(b) by a vertical dashed line of the same color as the corresponding mode number. As can be seen, for modes from $n = 2$ to $n = 4$, the predicted critical $a/L_{T_{\rm i}}$ values match very well with the GENE results. Their frequencies merge into the KTI gap frequency $\omega_{\rm KTI}$, which is the accumulation frequency of the BAE branch as pointed out in Ref. [13]. However, an extra $n = 1$ mode emerges before the growth rate of the $n = 1$ mode drops to zero with decreasing $a/L_{T_{\rm i}}$. To get a closer look at this, the KBM and BAE branches plus the continua solutions of the GFLDR for $n = 1$ are shown in Fig. 7(a). It can be seen that the KBM branch is stabilized with increasing $a/L_{T_{\rm i}}$ and the BAE branch becomes unstable when $a/L_{T_{\rm i}}$ surpasses a certain threshold. Note that near $\delta W_{\rm f} \to 0$, the solutions to Eq. (10) pile up near the accumulation point, which justifies the assumption above that the value of $\delta W_{\rm f}$ is arbitrary. Indeed, by solving Eq. (10) fixing $\delta W_{\rm f} = -0.01$ and varying $a/L_{T_{\rm i}}$, it can be seen in Fig. 7(b) that results of GENE simulations match very well with solutions of the GFLDR in both small and large $a/L_{T_{\rm i}}$ regions. Although there are some small differences in the values of growth rates and frequencies, it is believed that these differences are acceptable because deviations of the same order can be found when we merely change the geometry, as can be seen by comparing the blue solid lines and dashed lines in Figs. 7(b1) and 7(b2). Based on the above comparison with all these similarities in both mode structure and parameters dependences, we conclude that the low-n mode found in GENE simulations in HL-2A plasma is the BAE branch of the SAW spectrum described by the GFLDR (Eq. (10)).

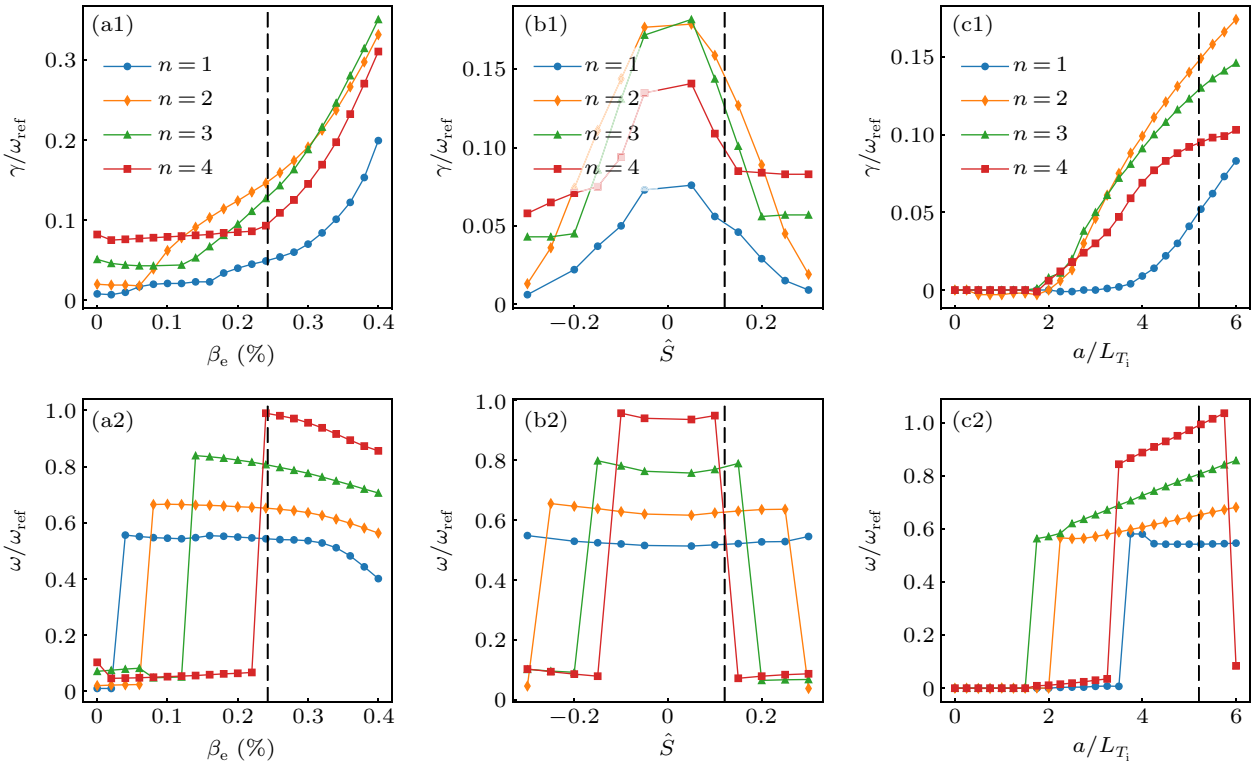


Fig. 4. The growth rate (upper panel) and corresponding frequency (lower panel) of linear GENE simulations for parametric scans of $\beta_{\rm e}$ (effectively the total β), $\hat{s}$ and $a/L_{T_{\rm i}}$, respectively. The black dashed lines indicate the nominal values.

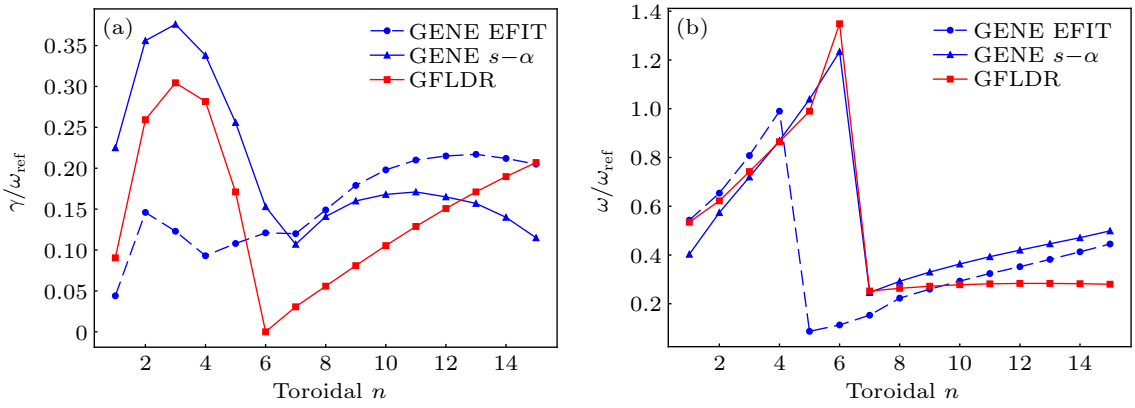


Fig. 5. The results of NFI GENE simulations using EFIT equilibrium and $\hat{s}$–α geometry and GFLDR solutions: (a) growth rates and (b) frequencies.

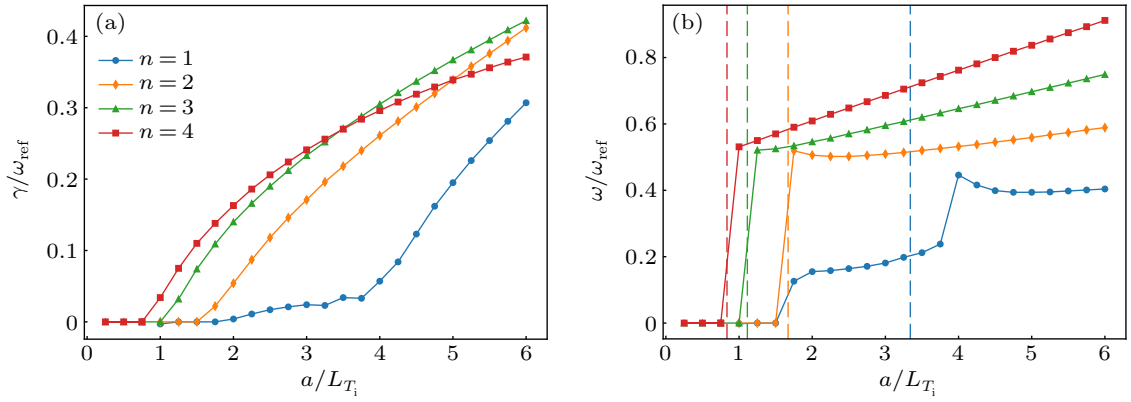


Fig. 6. The growth rate (a) and frequency (b) of the GENE when $a/L_{T_{\rm i}}$ is scanned for modes from $n=1$ to $n=4$ using s–α geometry. The vertical dashed line indicates the critical value calculated using Eq. (12). The same color indicates the same mode number n.

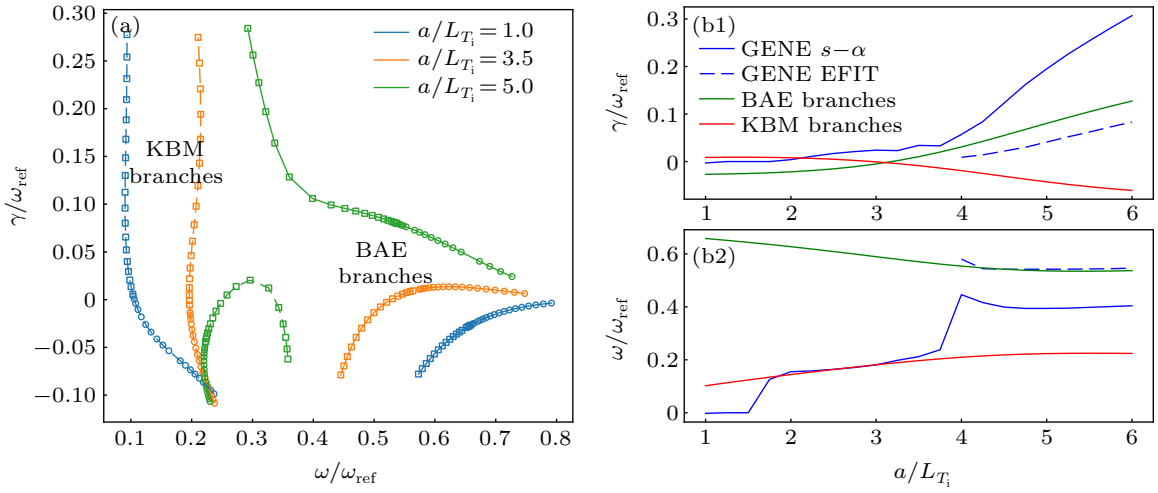


Fig. 7. (a) The KBM branches and BAE branches, i.e., lines marked by squares on the left and right, respectively, are shown connected to the continua solutions of the GFLDR marked by circles. To obtain the KBM and BAE branches, $\delta W_{\rm f}$ is scanned from -0.1 to 0, $a/L_{T_{\rm i}}=1.0$, 3.5 and 5.0 are chosen and Eq. (10) is solved. To obtain the continua solutions, $k_{\parallel}qR$ is scanned from 0 to 0.1 and $\Lambda=\pm k_{\parallel}qR$ is solved. (b1) The growth rates of the GENE result and that of the BAE/KBM branch near accumulation points are shown when $a/L_{T_{\rm i}}$ is scanned. (b2) Same as (b1) but frequencies are shown.

3.2. The case with fast ions

When fast ions are included in the GENE simulations, the growth rates reduce over the whole k_y spectrum as shown in Fig. 2. It is clarified in the following that the reduction of the growth rate in the ITG region is ascribed to fast ion dilution effects through direct comparison with the dispersion relation derived from GENE equations.

In order to simplify the gyrokinetic Vlasov equation (Eq. (1)) and derive a dispersion relation suitable for the description of the fast ion dilution effect, the so-called 'local kinetic limit',[21] i.e., the assumption that fluctuation fields are well localized near $z=0$, is introduced. Hence, the z deriva-

tives of fluctuation terms can be replaced by the parallel wave number

$$\mathrm{i}k_{\parallel} = \frac{1}{JB_0}\frac{\partial}{\partial z}. \tag{13}$$

This assumption is well satisfied by modes with large toroidal mode number n. Meanwhile, near $z = 0$, the z derivative of the equilibrium field satisfies

$$\partial_z B_0 \propto \frac{a}{R}\sin(z) \to 0, \tag{14}$$

so that the $v_{\parallel}$ derivative terms multiplied by $\partial_z B_0$ can be neglected. Then, the simplified dimensionless gyrokinetic equation can be expressed as follows:

$$\left(\omega - k_{\parallel}v_{Tj}v_{\parallel} - \tilde{\omega}_{\mathrm{D}} - \frac{T_j}{Z_j}v_{\parallel}^2\beta_{\mathrm{e}}\frac{p_0}{B_0^2}\omega_{\mathrm{p}}k_y\right)\Gamma_j$$
$$= (\omega + \tilde{\omega}_{*j})\frac{Z_j}{T_j}f_{0j}\bar{\chi}_{1j}, \tag{15}$$

where

$$\tilde{\omega}_{*j} = \frac{T_j}{Z_j}k_y[\omega_{nj} + \omega_{Tj}((v_{\parallel}^2 + \mu B_0 - 3/2)], \tag{16}$$

$$\tilde{\omega}_{\mathrm{D}} = (2v_{\parallel}^2 + \mu B_0)\frac{T_j}{Z_j}\frac{(\boldsymbol{k}_{\perp}\times\boldsymbol{B}_0)\cdot\nabla B_0}{B_0^3} \tag{17}$$

correspond to the diamagnetic frequency and the magnetic drift frequency respectively. Neglecting the collisional effect and parallel magnetic fluctuations for simplicity, equation (15) is combined with the quasi-neutrality condition

$$\sum_j \pi n_j Z_j \int B_0\bar{\Gamma}_j \mathrm{d}v_{\parallel}\,\mathrm{d}\mu = \phi_1\sum_j\frac{Z_j^2 n_j}{T_j}, \tag{18}$$

and the parallel Ampère law

$$\sum_j \frac{\beta_{\mathrm{e}}}{2}v_{Tj}\pi n_j Z_j\int B_0\bar{\Gamma}_j v_{\parallel}\,\mathrm{d}v_{\parallel}\,\mathrm{d}\mu = k_{\perp}^2 A_{1\parallel}. \tag{19}$$

In derivations of Eqs. (18) and (19) from Eqs. (2) and (3), we have replaced f_{1j} by the non-adiabatic distribution Γ_j. In the local version of GENE, the gyro-averaging of a quantity, ϕ_1 for example, is equivalent to multiplying it by the zeroth-order Bessel function J_0 (see Appendix A in Ref. [22]), which means

$$\bar{\phi}_1 = J_0(\sqrt{2b_j\mu B_0})\phi_1, \tag{20}$$

where $b_j = k_{\perp}^2 m_j T_{0j}/(Z_j^2 B_0^2)$. Substituting Eq. (15) and the expression of gyro-average operation Eq. (20) into Eqs. (18) and (19), a set of kinetic eigenmode equations for ϕ_1 and $A_{1\parallel}$ can be thus obtained

$$\sum_j\frac{Z_j^2 n_j}{T_j}P_j^0\phi_1 - \sum_j\frac{Z_j^2 n_j}{T_j}P_j^1 v_{Tj}A_{1\parallel} = \sum_j\frac{Z_j^2 n_j}{T_j}\phi_1, \tag{21}$$

$$\sum_j\frac{\beta_{\mathrm{e}}}{2}v_{Tj}\frac{Z_j^2 n_j}{T_j}P_j^1\phi_1 - \sum_j\frac{\beta_{\mathrm{e}}}{2}v_{Tj}\frac{Z_j^2 n_j}{T_j}P_j^2 v_{Tj}A_{1\parallel} = k_{\perp}^2 A_{1\parallel}, \tag{22}$$

where P_j^{m} is defined as

$$P_j^{\mathrm{m}} = \int\frac{(\omega + \tilde{\omega}_{*j})J_0^2(\sqrt{2b_j\mu B_0})f_{0j}}{\left(\omega - k_{\parallel}v_{Tj}v_{\parallel} - \tilde{\omega}_{\mathrm{D}} - \frac{T_j}{Z_j}v_{\parallel}^2\beta_{\mathrm{e}}\frac{p_0}{B_0^2}\omega_{\mathrm{p}}k_y\right)}\pi B_0 v_{\parallel}^{\mathrm{m}}\,\mathrm{d}v_{\parallel}\,\mathrm{d}\mu. \tag{23}$$

It can be easily shown that by setting $\beta_{\mathrm{e}} = 0$, equation (21) is reduced to the dispersion relation of the ITG mode in the electrostatic limit derived Ref. [21]. As will be shown below, the frequencies and growth rates of the high-n modes ($n = 16$ for example) in our case can be reproduced by this dispersion relation with a small relative error, so we confirm that the dominant modes in the range of $0.2 < k_y < 1$ in Fig. 2 are typically ITG modes. Once the parallel wave number $k_{\parallel}$ is chosen, the eigenvalue ω can be numerically solved by combining Eqs. (21) and (22). In order to determine $k_{\parallel}$ and make direct comparison with GENE simulations, the eigenmode structures here, i.e., the shapes of normalized ϕ_1 and $A_{1\parallel}$, are assumed to be similar to those in the above case without fast ions. Then, $k_{\parallel}$ is determined by solving Eq. (15) without fast ions and kept unchanged afterwards. Under this assumption, the dispersion relation can be obtained by setting the determinant of the combination of Eqs. (21) and (22) to be zero. Focusing on the high-n modes, for example taking $n = 16$ ($k_y\rho_{\mathrm{ref}} = 0.5$) for the HL-2A case, when the fast ion fraction is increased from 0 to 0.3, the growth rates solved from Eqs. (21) and (22) are shown in Fig. 8 and compared with results of GENE simulations. In order to rule out the contribution of fast ions, $P_{\mathrm{fi}}^{\mathrm{m}}$ are forced to be zero and the results are shown by dashed lines in Fig. 8. Two cases may be of interest. Case 1 keeps both the density gradient $a/L_{n_{\mathrm{fi}}}$ and temperature gradient $a/L_{T_{\mathrm{fi}}}$ of fast ions at low values, i.e., the same gradients as in Table 1. Meanwhile, case 2 uses relatively high values for the fast ion gradients, i.e., $a/L_{n_{\mathrm{fi}}} = 1.4$ and $a/L_{T_{\mathrm{fi}}} = 4.0$. As can be seen in Fig. 8, the results of GENE simulations and the solutions of dispersion relation match well with each other. The relative errors are under 10%, which may mainly result from the neglect of collision effects and parallel magnetic fluctuation in the derivation of the dispersion relation. The fast ion dilution effect can be explained by comparing the dashed lines with solid lines as well as case 1 with case 2 in Fig. 8. It can be seen for the cases with low fast ion gradient that the contribution of fast ions is nearly negligible. The change in thermal ion density is responsible for the reduction in the growth rate with increasing fast ion density. The same dependence can be checked from Eqs. (21) and (22). Characterized by its high temperature and low density, the fast ion effect influences the dispersion relation via a small factor $n_{\mathrm{fi}}/T_{\mathrm{fi}}$. Hence, when the fast ion gradient as the driving force in $P_{\mathrm{fi}}^{\mathrm{m}}$ is not large enough, $P_{\mathrm{fi}}^{\mathrm{m}}\cdot n_{\mathrm{fi}}/T_{\mathrm{fi}}$ are negligible and fast ions govern the dispersion relation mainly by changing the thermal ion parameters rather than by themselves.

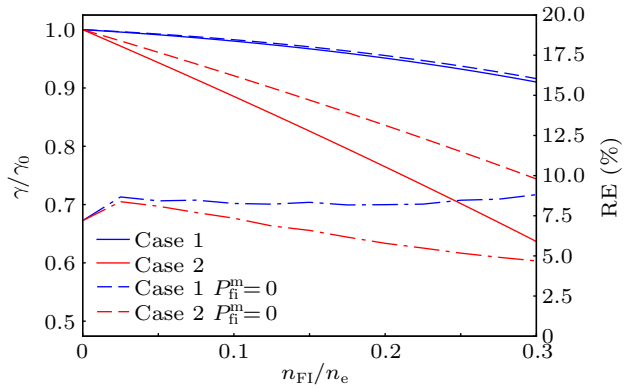


Fig. 8. The growth rates solved by the determinant of Eqs. (21) and (22) for case 1 and case 2 are shown by blue and red solid lines respectively, and normalized to the growth rate of the case without fast ions. The dashed lines show the solutions when fast ion contributions are ruled out. The dotted-dashed lines show the relative error (RE) between the complex solutions of our dispersion relation and the results of GENE simulations with the same parameters.

4. Summary

In this work, low-n Alfvénic modes, which are frequently observed in fast-ion-relevant tokamak discharges, were investigated numerically in HL-2A NBI-heated plasma. The local version of the GENE code was employed to perform simulations on the linear stability of NBI-heated plasma. High-frequency electromagnetic low-n modes were observed in the simulations of HL-2A plasma excluding fast ions. By comparing comprehensive linear GENE simulation results with the solutions of the general fish-bone-like dispersion relation derived in Ref. [13], it was found that their linear stability properties match well with the BAE branch of the shear Alfvénic spectrum. By investigating the mode structure and scanning numerical parameters, it has been shown that these low-n modes are destabilized only by a large ion temperature gradient combined with relatively weak magnetic shear. In the case including fast ions, a finite reduction in the growth rate was observed over the whole k_y spectrum. By solving a dispersion relation derived directly from simplified GENE equations, it was demonstrated that the linear stabilization role of fast ions on the ITG mode can be ascribed to the dilution mechanism.

Acknowledgments

The authors would like to thank D. L. Yu, K. R. Fang, X. X. He, Z. J. Li, and X. Zhang for their help in providing experimental data from the HL-2A tokamak. Project supported by the National Key Research and Development Program of China (Grant No. 2017YFE0301201) and also partially by the National Natural Science Foundation of China (Grant Nos. U1967206 and 11775069).

References

[1] Mantica P, Strintzi D, Tala T, Giroud C, Johnson T, Leggate H, Lerche E, Loarer T, Peeters A G and Salmi A 2009 *Phys. Rev. Lett.* **102** 175002

[2] Mantica P, Angioni C, Challis C, Colyer G, Frassinetti L, Hawkes N, Johnson T, Tsalas M, Devries P C and Weiland J 2011 *Phys. Rev. Lett.* **107** 135004

[3] Citrin J, Jenko F, Mantica P, Told D, Bourdelle C, Garcia J, Haverkort J W, Hogeweij G M D, Johnson T and Pueschel M J 2013 *Phys. Rev. Lett.* **111** 155001

[4] Citrin J, Garcia J, Görler T, Jenko F, Mantica P, Told D, Bourdelle C, Hatch D R, Hogeweij G M D, Johnson T, Pueschel M J, Schneider M and JET-EFDA Contributors 2014 *Plasma Phys. Control. Fusion* **57** 014032

[5] Garcia J, Challis C, Citrin J, Doerk H, Giruzzi G, Görler T, Jenko F, Maget P and JET Contributors 2015 *Nucl. Fusion* **55** 053007

[6] Garcia J, Grler T and Jenko F 2018 *Phys. Plasmas* **25** 055902

[7] Siena A Di, Görler T, Doerk H, Poli E and Bilato R 2018 *Nucl. Fusion* **58** 054002

[8] Jenko F, Dorland W, Kotschenreuther M and Rogersa B N 2000 *Phys. Plasmas* **7** 1904

[9] Nocente M, Kazakov Ye O, Garcia J, *et al.* 2020 *Nucl. Fusion* **60** 124006

[10] Kazakov Ye O, Ongena J, Wright J C, *et al.* 2021 *Phys. Plasmas* **28** 020501

[11] Mazzi S, Garcia J, Zarzoso D, Kazakov Ye O, Ongena J, Görler T, Nocente M, Dreval M, Stancar M, Szepesi G, Eriksson J, Sahlberg A and Benkadda S 2020 arXiv: 2010.07977

[12] Yu D L, Wei Y L, Liu L, *et al.* 2016 *Nucl. Fusion* **56** 056003

[13] Zonca F, Chen L and Santoro R A 1996 *Plasma Phys. Control. Fusion* **38** 2011

[14] Görler T, Lapillonne X, Brunner S, Dannert T, Jenko F, Merz F and Told D 2012 *Journal of Computational Physics* **230** 7053

[15] Shi Z B, Jiang M, Huang X L, Zhong W L, Chen W, Che Y L, Liu Z T, Ding X T, Yang Q W and Duan X R 2014 *Rev. Sci. Instrum.* **85** 023510

[16] Wei Y L, Yu D L, Liu L, Ida K, Hellermann M V, Cao J Y, Sun A P, Ma Q, Chen W J, Liu Y, Yan L W, Yang Q W, Duan X R and Liu Y 2014 *Rev. Sci. Instrum.* **85** 103503

[17] Pankin A, McCune D, Andre R, Bateman G and Kritz A 2004 *Computer Physics Communications* **159** 157

[18] Connor J W, Hastie R J and Taylor J B 1978 *Phys. Rev. Lett.* **40** 396

[19] Zonca F and Chen L 2014 *Phys. Plasmas* **21** 072120

[20] Manickam J and Pomphrey N 1987 *Nucl. Fusion* **27** 1461

[21] Kim J Y, Horton W and Dong J Q 1993 *Phys. Fluids B* **5** 4030

[22] Merz F 2008 *Gyrokinetic Simulation of Multimode Plasma Turbulence* (Ph.D. Dissertation) (University of Münster)

[23] Told D 2012 *Gyrokinetic Microturbulence in Transport Barriers* (Ph.D. Dissertation) (University of Ulm)